Article

Continuum–Discontinuum Bonded-Block Model for Simulating Mixed-Mode Fractures

Yue Sun *, Tao Chen, Longquan Yong and Qian Chen

School of Mathematics and Computer Science, Shaanxi University of Technology, Hanzhong 723001, China; chentao@snut.edu.cn (T.C.); yonglongquan@126.com (L.Y.); chenqian@snut.edu.cn (Q.C.)
* Correspondence: sunyue@snut.edu.cn

Abstract: In this study, an improved discontinuous deformation analysis method with sub-block strategy is introduced to numerically simulate mixed-mode fractures. This approach partitions the material domain into continuum and potential discontinuum regions, applying specialized modeling techniques to each. In the continuum region, penalty-like bonding springs are employed to glue the sub-blocks together to capture the elastic behavior of the material. In the potential discontinuum region, the cohesive springs with the stiffness based on the cohesive zone model are implemented between sub-blocks to reproduce the process of crack nucleation and propagation. The primary advantage of this method is its capability to effectively model the transition of quasi-brittle solids from a continuous to a discontinuous stage through the degradation of cohesive springs. This accurately represents material failure while maintaining stability and consistency along uncracked interfaces. Another significant benefit is the method's efficiency, as it avoids complex contact operations along sub-block interfaces before the cohesive spring between them fails. Validation through various benchmark numerical examples, such as cantilever beam-bending and diverse fracture simulations, demonstrates the method's accuracy and robustness by comparing the results with analytical solutions. These comparisons show that the proposed method effectively captures the interplay between tensile and shear traction components in the mixed-mode crack propagation process.

Keywords: quasi-brittle fracture; discontinuous deformation analysis (DDA); sub-block; cohesive zone model; cohesive contact spring

MSC: 74H15; 65N22; 74R10

1. Introduction

The robust and accurate simulation of fracture propagation phenomena is of paramount importance across a wide range of applications ranging from material science to geotechnique engineering. Among the multitude of fracture modes encountered, mixed-mode fractures, characterized by the simultaneous presence of tensile and shear components, pose challenges due to their inherent complexity and the intricacies involved in capturing the interplay between these competing fracture mechanisms.

In recent decades, researchers have proposed various analytical [1–4], experimental [5–7], and numerical approaches [8–12] to tackle this challenge. Among these, numerical methods offer advantages in terms of cost-effectiveness and efficiency. According to the spatial discretization manner adopted, the numerical methods are usually categorized into continuum-based and discontinuum-based methods [13,14].

Continuum-based methods typically employ grid lines to discretize the domain of interest into finite elements. Combined with appropriate failure criteria, these methods possess high accuracy in computing material deformation and stress distribution, enabling them to accurately predict fracture behavior in static or quasi-static problems. However, in dynamic problems, they encounter difficulties with large-scale opening and sliding along

discontinuous material interfaces. To address these challenges, the extended finite element method (XFEM) [15,16] and the numerical manifold method (NMM) [17,18] were proposed as potential solutions. Nonetheless, simulating multi-crack problems remains a complex task for these methods.

In contrast, discontinuum-based approaches typically represent the material as an assembly of individual particles or blocks. The distinct element method (DEM) and the discontinuous deformation analysis (DDA) [19,20] are two widely employed techniques within this category. Depending on the elemental computing unit, the DEM is implemented in two primary forms: the bonded-particle model [21,22] and bonded-block model (BBM) [23,24]. By interconnecting adjacent particles/blocks with contact springs, these two models enable the DEM to reproduce the material failure process. Similarly, the DDA simulates fracturing progress by introducing the sub-block strategy [25] to subdivide intact blocks into smaller sub-blocks and connect them together by point contact springs [26,27] or distributed bonds [28–30]. These kinds of approaches are well known as the sub-block DDA (SDDA) method.

In recent years, coupling continuum–discontinuum approaches have been emerging as a powerful technique in fracture modeling, such as finite–discrete element methods [31–37] and FEM–DDA coupling approaches [38–42]. These methods discretize each discrete element/block into finite elements, leveraging the high computational efficiency of continuum methods for intact regions and the ability of discontinuum methods to capture discontinuities and fracture processes. By judiciously integrating these complementary techniques, researchers aim to develop robust and accurate numerical frameworks for simulating complex mixed-mode fracture problems. However, these methods may also face the difficulties of distorted mesh and remeshing operation due to the introduction of finite element approximation within continuum regions.

In our previous work [43], we introduced so-called bonding springs (BSs) in the SDDA to enhance the accuracy of block deformation and stress distribution predictions. This enriched method models each block as an assembly of triangular sub-blocks, utilizing BSs to glue adjacent sub-blocks together along their interfaces. This approach ensures continuity and consistency within each block and avoids the need for contact operations between sub-blocks inside a block, thus enabling more efficient computation. However, BSs have identical normal and shear stiffness, limiting their ability to simulate solids subjected to both tensile and tangential tractions, especially in mixed-mode failures.

In this paper, we propose a continuum–discontinuum bonded-block model (CDBBM) to numerically reproduce mode-I, mode-II, and mixed-mode crack processes. Inspired by the study [41], we adopted a partitioning of the material domain into two distinct subdomains: the continuum region and the potential discontinuum region. The mechanical response within each subdomain was calculated using specialized modeling techniques.

Regarding the continuum region, where the material remains intact and undergoes elastic deformation, the subdomain is discretized into sub-blocks. Adjacent sub-blocks are glued together by a BS at their vertices. BSs remain installed throughout the computation, capturing the elastic behavior of the solid under various loading conditions.

Regarding the potential discontinuum region, where material failure may occur, this subdomain serves as a transitional zone between the continuum and fully discontinuum states. Consequently, this region is subdivided into sub-blocks connected by a pair of normal and shear cohesive springs (CSs) along the sub-block interfaces. The discrete cohesive zone model (CZM), proposed by Xie et al. [9], is employed as the constitutive relation for these CSs, allowing for the gradual degradation of material properties and the nucleation of new cracks as deformation progresses. When the effective opening of a CS exceeds the peak value, a new crack forms, and contact operations are initiated along the crack surfaces.

Diversified benchmark numerical experiments are conducted to validate the accuracy and robustness of the CDBBM. First, we assess the fidelity of our approach in capturing continuum deformation by examining the cantilever beam-bending problem using differ-

ent quadrilateral finite-element-type meshes. Then, we evaluate the performance of the CDBBM in pure and mixed-mode fracture simulations. The numerical results obtained by the CDBBM are compared against analytical solutions, demonstrating the efficacy and reliability of the proposed method.

2. Framework of the CDBBM

2.1. Spatial Discretization

The CDBBM subdivides the material domain into a continuum subdomain (C-domain) and a potential discontinuum subdomain (D-domain) to reduce computational costs, such as remeshing and contact interactions. Such subdivision can be done in a relatively coarse manner. As a result, the CDBBM approach relies somewhat on the a priori knowledge of the mechanical response of the material. The schema shown in Figure 1a is taken as an illustrative example. The material domain is partitioned into two regions, the left as the C-domain (in yellow) and the right as the D-domain (in purple). In the CDBBM, both of the regions are further subdivided into sub-blocks connected by two different types of springs according to the region where sub-block interfaces are embedded, as shown in Figure 1b.
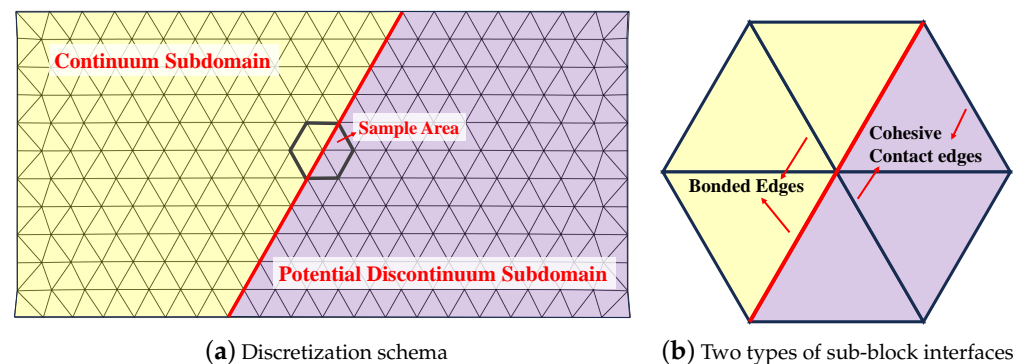

(**a**) Discretization schema   (**b**) Two types of sub-block interfaces

Figure 1. Discretization diagram of CDBBM for continuum subdomain and potential discontinuum subdomain.

Within the C-domain, the adjacent edges of the sub-blocks are bonded by bonding springs (BSs) at their overlapping vertices. These BSs are continuously installed throughout the entire computational process to maintain the displacement continuity. Furthermore, BSs are also implemented along the common boundary of the C-domain and D-domain to prevent the erroneous prediction of cracks.

In contrast, the opposing edges of the sub-blocks within the D-domain are connected by cohesive springs (CSs) based on the cohesive zone model (CZM), along their interfaces. Adopting a specific TSL as the constitutive relation, CSs represent the fracture behavior through its failure process, encompassing the hardening stage, softening stage, and complete fracture. To avoid unnecessary contact calculations before crack initiation, the connection information for CSs is maintained through an array. Once a CS fails, it is subsequently removed from the data structure.

2.2. Displacement Approximation

The CDBBM discretizes both the C-domain and D-domain into sub-blocks. The displacement vector
$u(x)$, $x = (x, y)$, within the *i*-th sub-block has the following approximation in matrix form:

$$u(x) = \begin{pmatrix} u_x \\ u_y \end{pmatrix} = T_i a_i, \tag{1}$$

where $\boldsymbol{a}_i = (a_1, a_2, a_3, a_4, a_5, a_6)^\top$ is the unknown vector to be determined on the considered sub-block, and $\boldsymbol{T}_i$ represents the displacement mode matrix, i.e.,

$$\boldsymbol{T}_i = \begin{pmatrix} T_{11} & T_{12} & T_{13} & T_{14} & T_{15} & T_{16} \\ T_{21} & T_{22} & T_{23} & T_{24} & T_{25} & T_{26} \end{pmatrix}, \tag{2}$$

where $T_{11} = T_{22} = 1$, $T_{12} = T_{15} = T_{21} = T_{24} = 0$, $T_{13} = -T_{25} = y_0 - y$, $T_{14} = T_{23} = x - x_0$, $T_{16} = (y - y_0)/2$, and $T_{26} = (x - x_0)/2$, in which (x_0, y_0) is the sub-block barycenter.

For the first-order approximation, as adopted in Equation (1), the components of the unknown vector $\boldsymbol{a}_i$ have the following physical interpretations: a_1 and a_2 indicate the translational displacement along the x and y axes, respectively, and a_3 denotes the rotation angle of the i-th sub-block about its barycenter, while a_4 and a_5 represent normal strain components of the sub-block, and a_6 is its shear strain component.

2.3. Equilibrium Equations

The CDBBM subdivides the material domain, say Ω bounded by Γ, into a C-domain and a D-domain and further discretizes the two regions into sub-blocks, which make up a sub-block system. Minimizing the system's potential energy leads to the following global equilibrium equations in the matrix form:

$$\boldsymbol{M}\ddot{\boldsymbol{a}} + \boldsymbol{K}\boldsymbol{a} = \boldsymbol{f}, \tag{3}$$

where $\boldsymbol{a}$ assembles all of the unknowns of the sub-block system, $\boldsymbol{M}$ stand for the mass matrix, and the stiffness matrix $\boldsymbol{K}$ and the right-hand side $\boldsymbol{f}$ are the summations below:

$$\boldsymbol{K} = \overline{\boldsymbol{K}} + \boldsymbol{K}_c + \boldsymbol{K}_{\mathrm{BS}} + \boldsymbol{K}_{\mathrm{CS}}, \quad \boldsymbol{f} = \overline{\boldsymbol{f}} + \boldsymbol{f}_\Gamma + \boldsymbol{f}_c + \boldsymbol{f}_{\mathrm{BS}} + \boldsymbol{f}_{\mathrm{CS}}. \tag{4}$$

$\overline{\boldsymbol{K}}, \boldsymbol{K}_c, \boldsymbol{K}_{\mathrm{BS}}$, and $\boldsymbol{K}_{\mathrm{CS}}$ represent the sub-block stiffness matrix, contact spring stiffness matrix, and the BS and CS stiffness matrices, respectively, and, additionally, $\overline{\boldsymbol{f}}$ indicates the summation of sub-block initial forces and body force vectors, $\boldsymbol{f}_c$ is the contact spring force vector, and $\boldsymbol{f}_\Gamma$ is the vector contributed to by the boundary constraints, such as fixed-point springs and traction forces; $\boldsymbol{f}_{\mathrm{BS}}$ and $\boldsymbol{f}_{\mathrm{CS}}$ are the spring force vectors of BS and CS, respectively.

In order to solve the ordinary differential equations in Equation (3), we apply Taylor's expansion method for $\boldsymbol{a}$ at $t = t_n$ with the time step size Δt, i.e.,

$$\boldsymbol{a}^n \equiv \boldsymbol{a}(t_n) = 0, \quad \boldsymbol{a}^{n+1} \equiv \boldsymbol{a}(t_{n+1}) = \boldsymbol{a}(t_n + \Delta t), \tag{5}$$

$$\boldsymbol{a}^{n+1} = \boldsymbol{a}^n + \Delta t \dot{\boldsymbol{a}}^n + \frac{\Delta t^2}{2}\ddot{\boldsymbol{a}}^n = \Delta t \dot{\boldsymbol{a}}^n + \frac{\Delta t^2}{2}\ddot{\boldsymbol{a}}^n. \tag{6}$$

Assuming that the acceleration remains constant during each time step, we have

$$\ddot{\boldsymbol{a}}^{n+1} = \ddot{\boldsymbol{a}}^n = \frac{2}{\Delta t^2}\left(\boldsymbol{a}^{n+1} - \dot{\boldsymbol{a}}^n \Delta t\right). \tag{7}$$

Substituting Equation (7) into Equation (3) leads to

$$\left(\frac{2}{\Delta t^2}\boldsymbol{M} + \boldsymbol{K}\right)\boldsymbol{a}^{n+1} = \boldsymbol{f} + \frac{2}{\Delta t^2}\boldsymbol{M}\dot{\boldsymbol{a}}^n. \tag{8}$$

Details about the matrices $\boldsymbol{M}, \overline{\boldsymbol{K}}, \boldsymbol{K}_c, \overline{\boldsymbol{f}}, \boldsymbol{f}_c$, and $\boldsymbol{f}_\Gamma$ appearing in Equations (4) and (8) can be found in our previous work [43]. Furthermore, we will give the matrices $\boldsymbol{K}_{\mathrm{BS}}, \boldsymbol{K}_{\mathrm{CS}}, \boldsymbol{f}_{\mathrm{BS}}$, and $\boldsymbol{f}_{\mathrm{CS}}$ in the following sections.

3. Formulas of Bonding Springs (BSs)

The CDBBM installs BSs between the vertexes of adjacent sub-blocks to retain the displacement continuity throughout the C-domain. As shown in Figure 2, S_i and S_j are

two sub-blocks connected by a BS between the vertex P and Q. We assume that P and Q are located at p^n and q^n at t_n. Using d^n and d^{n+1} to represent the relative displacement between P and Q at t_n and t_{n+1}, respectively, we have

$$d^n = p^n - q^n, \tag{9}$$

$$d^{n+1} = p^{n+1} - q^{n+1} = (p^n + u_p^{n+1}) - (q^n + u_q^{n+1}) = d^n + (u_p^{n+1} - u_q^{n+1}), \tag{10}$$

where u_p^{n+1} and u_q^{n+1} are the displacement of P and Q during the $(n+1)$-th time step. We substitute Equation (1) into Equation (10), and we have

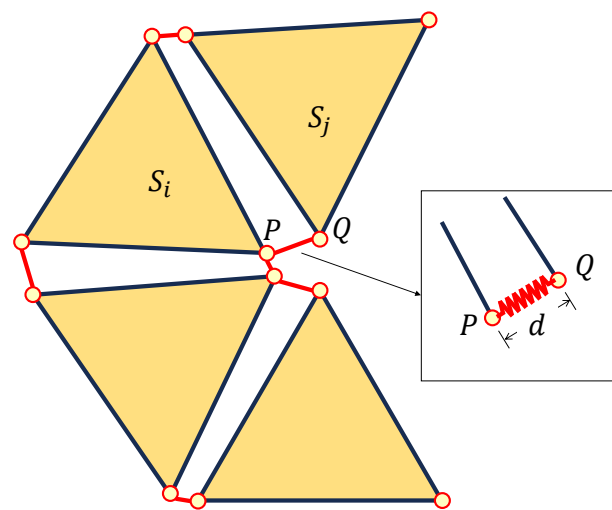$$d^{n+1} = d^n + T_i a_i^{n+1} - T_j a_j^{n+1}, \tag{11}$$

Figure 2. Schematic diagram of BSs that glue adjacent sub-blocks within the C-domain.

The BS's strain energy Π_{BS} can be computed by

$$\Pi_{\mathrm{BS}} = \frac{1}{2} k_{\mathrm{BS}} \left(d^{n+1} \right)^2, \tag{12}$$

where k_{BS} denotes the stiffness of BSs. We substitute Equation (11) into Equation (12), and we obtain the derivatives of Π_{BS} with respect to a_i and a_j, i.e.,

$$\frac{\partial^2 \Pi_{\mathrm{BS}}}{\partial a_i^\top \partial a_i} = k_{\mathrm{BS}} T_i^\top T_i \rightarrow K_{ii}, \qquad \frac{\partial^2 \Pi_{\mathrm{BS}}}{\partial a_j^\top \partial a_j} = k_{\mathrm{BS}} T_i^\top T_i \rightarrow K_{jj}, \tag{13}$$

$$\frac{\partial^2 \Pi_{\mathrm{BS}}}{\partial a_i^\top \partial a_j} = -k_{\mathrm{BS}} T_i^\top T_i \rightarrow K_{ij}, \qquad \frac{\partial^2 \Pi_{\mathrm{BS}}}{\partial a_j^\top \partial a_i} = -k_{\mathrm{BS}} T_i^\top T_i \rightarrow K_{ji}, \tag{14}$$

$$-\frac{\partial \Pi_{\mathrm{BS}}}{\partial a_i} = k_{\mathrm{BS}} T_i^\top d^n \rightarrow f_i, \qquad -\frac{\partial \Pi_{\mathrm{BS}}}{\partial a_j} = -k_{\mathrm{BS}} T_i^\top d^n \rightarrow f_j, \tag{15}$$

where a_i and a_j indicate a_i^{n+1} and a_j^{n+1}, respectively, whose superscripts are omitted for convenience. The matrices K_{ii}, K_{ij}, K_{ji}, and K_{jj} in the above equations are assembled into K_{BS} in Equation (4), and the vectors f_i and f_j are accordingly assembled into f_{BS}.

4. Formulas of Cohesive Springs (CSs)

The CDBBM incorporates CSs along the interfaces of sub-blocks within the D-domain. The stiffness of a CS is variable, contingent upon the separation between the two vertices

interconnected by the CS. A bi-linear traction–separation law (TSL) is adopted to define the CS stiffness. Consequently, the fracture process between two sub-blocks consists of an increase of the traction up to the peak value and a subsequent decrease until a complete failure occurs.

4.1. Potential Energy of CSs

As shown in Figure 3, we take the CS between P_1 and P_4 as an example. We assume that the normal opening and shear opening of the CS are d_r and d_s, respectively. The strain energy Π_{CS} can be computed by the summation below:

$$\Pi_{\text{CS}} = \frac{1}{2}k_r d_r^2 + \frac{1}{2}k_s d_s^2, \tag{16}$$

where k_r and k_s are the normal and shear stiffness, respectively.

The matrices derived from the derivatives of Π_{CS} with respect to the unknowns will be added to $\boldsymbol{K}_{\text{BS}}$ and $\boldsymbol{f}_{\text{BS}}$ in Equation (3). To this end, we first compute d_r and d_s. Since P_1, P_2, and P_3 move in each time step, the opening d_r and d_s have to be figured out based on the current configuration but not that of the previous time step.
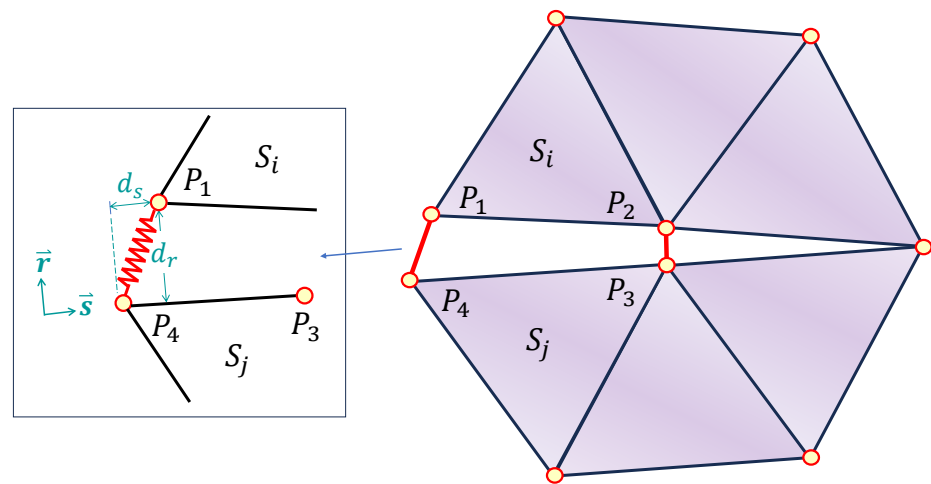

Figure 3. Schematic diagram of CSs that connect adjacent sub-blocks within the D-domain.

4.2. Normal Opening

We assume that the vertex P_m is located at $\boldsymbol{x}_m(x_m, y_m)$ at t_n, $m = 1, 2, 3, 4$, $n = 1, 2, \ldots$, and it moves with the displacement $\boldsymbol{u}_m(u_m, v_m)$ at t_{n+1}. From Figure 3, the normal opening at t_{n+1} is

$$d_r^{n+1} = \frac{\left|\overrightarrow{P_1P_4} \times \overrightarrow{P_1P_3}\right|}{\left|\overrightarrow{P_3P_4}\right|} = \frac{1}{L}\begin{vmatrix} 1 & x_1^{n+1} & y_1^{n+1} \\ 1 & x_4^{n+1} & y_4^{n+1} \\ 1 & x_3^{n+1} & y_3^{n+1} \end{vmatrix}, \tag{17}$$

where

$$x_m^{n+1} \equiv x_m + u_m, \quad y_m^{n+1} \equiv y_m + v_m, \tag{18}$$

$$L \equiv \left|\overrightarrow{P_3P_4}\right| = \sqrt{(x_4^{n+1} - x_3^{n+1})^2 + (y_4^{n+1} - y_3^{n+1})^2}. \tag{19}$$

When adopting a small enough time step size, we can simplify Equation (17) into

$$d_n \approx \frac{A}{L'} + \frac{1}{L'}\left[\begin{pmatrix} y_4 - y_3 \\ x_3 - x_4 \end{pmatrix}^\top \boldsymbol{u}_1 + \begin{pmatrix} y_1 - y_4 \\ x_4 - x_1 \end{pmatrix}^\top \boldsymbol{u}_3 + \begin{pmatrix} y_3 - y_1 \\ x_1 - x_3 \end{pmatrix}^\top \boldsymbol{u}_4\right], \tag{20}$$

where

$$L' \approx \sqrt{(x_4 - x_3)^2 + (y_4 - y_3)^2}, \quad A = -x_1 y_3 + x_1 y_4 + x_3 y_1 - x_3 y_4 - x_4 y_1 + x_4 y_3. \quad (21)$$

Substituting Equation (1) into Equation (20) leads to

$$d_n = \frac{A}{L'} + e_i a_i^{n+1} + e_j a_j^{n+1}, \quad (22)$$

in which the coefficient vectors are

$$e_i = \frac{1}{L'} \begin{pmatrix} y_4 - y_3 \\ x_3 - x_4 \end{pmatrix}^\top T_i(x_1), \quad e_j = \frac{1}{L'} \begin{pmatrix} y_1 - y_4 \\ x_4 - x_1 \end{pmatrix}^\top T_i(x_3) + \frac{1}{L'} \begin{pmatrix} y_3 - y_1 \\ x_1 - x_3 \end{pmatrix}^\top T_i(x_4). \quad (23)$$

4.3. Shear Opening

From Figure 3, the shear opening in the $(n+1)$-th time step is

$$d_s = \frac{\overrightarrow{P_4 P_1} \cdot \overrightarrow{P_4 P_3}}{\overrightarrow{P_4 P_3}} = \frac{1}{L} \begin{pmatrix} x_3^{n+1} - x_4^{n+1} \\ y_3^{n+1} - y_4^{n+1} \end{pmatrix}^\top \begin{pmatrix} x_1^{n+1} - x_4^{n+1} \\ y_1^{n+1} - y_4^{n+1} \end{pmatrix}. \quad (24)$$

For a small enough time step, the relative displacement of sub-blocks S_i and S_j are accordingly small. In this case, we can simplify the above equation by

$$d_s \approx \frac{A}{L'} + \frac{1}{L'} \begin{pmatrix} x_3 - x_4 \\ y_3 - y_4 \end{pmatrix}^\top u_1 - \frac{1}{L'} \begin{pmatrix} x_4 - x_3 \\ y_4 - y_3 \end{pmatrix} u_4. \quad (25)$$

Substituting Equation (1) into Equation (25) leads to

$$d_s \approx \frac{A}{L'} + g_i a_i^{n+1} + g_j a_j^{n+1}, \quad (26)$$

where

$$g_i = \frac{1}{L'} \begin{pmatrix} x_3 - x_4 \\ y_3 - y_4 \end{pmatrix}^\top T_i(x_1), \quad g_j = \frac{1}{L'} \begin{pmatrix} x_4 - x_3 \\ y_4 - y_3 \end{pmatrix} T_j(x_4). \quad (27)$$

4.4. CS Matrices

We substitute Equations (22) and (26) into Equation (16), and we can obtain the derivatives of Π_{CS} with respect to a_i^{n+1} and a_j^{n+1}, using $a_i \equiv a_i^{n+1}$ and $a_j \equiv a_j^{n+1}$, i.e.,

$$\frac{\partial^2 \Pi_{CS}}{\partial a_i^\top \partial a_i} = k_r e_i^\top e_i + k_s g_i^\top g_i \rightarrow K_{ii}, \quad \frac{\partial^2 \Pi_{CS}}{\partial a_i^\top \partial a_j} = k_r e_i^\top e_j + k_s g_i^\top g_j \rightarrow K_{ij}, \quad (28)$$

$$\frac{\partial^2 \Pi_{CS}}{\partial a_j^\top \partial a_i} = k_r e_j^\top e_i + k_s g_j^\top g_i \rightarrow K_{ji}, \quad \frac{\partial^2 \Pi_{CS}}{\partial a_j^\top \partial a_j} = k_r e_j^\top e_j + k_s g_j^\top g_j \rightarrow K_{jj}, \quad (29)$$

$$-\frac{\partial \Pi_{CS}}{\partial a_i} = -\frac{k_r A}{L'} e_i - \frac{k_s A}{L'} g_i \rightarrow f_i, \quad -\frac{\partial \Pi_{CS}}{\partial a_j} = -\frac{k_r A}{L'} e_j - \frac{k_s A}{L'} g_j \rightarrow f_j, \quad (30)$$

in which K_{ii}, K_{ij}, K_{ji}, and K_{jj} are added to K_{CS} in Equation (4), and f_i and f_j are added to f_{CS}.

5. Normal/Shear Stiffness of CSs

In the CDBBM, the variation of CS stiffness are determined by the bi-linear TSL relation as shown in Figure 4. Here, some notations are used, including the mode-I and mode-II strain energy release rate G_I and G_{II}, the associated fracture energy G_{Ic} and G_{IIc}, the tensile

and shear cohesive strength σ_c and τ_c, the corresponding maximum opening δ_m and γ_m, and the critical separation δ_c and γ_c.

According to Figure 4, we have the following relations:

$$\delta_m = \frac{2G_{\mathrm{Ic}}}{\sigma_c}, \quad \gamma_m = \frac{2G_{\mathrm{IIc}}}{\tau_c}, \quad \delta_c = \frac{\sigma_c}{k_r^0}, \quad \gamma_c = \frac{\tau_c}{k_s^0}, \tag{31}$$

where k_r^0 and k_s^0 are the initial normal and shear CS stiffness, respectively. Xie et al. [9] have given the formulas below to determine their values:

$$k_r^0 = EBr, \quad k_s^0 = GBr, \tag{32}$$

in which E and G denote material's Young modulus and shear modulus, B is the thickness outside the plane, and r indicates the ratio of sub-block width to its height.
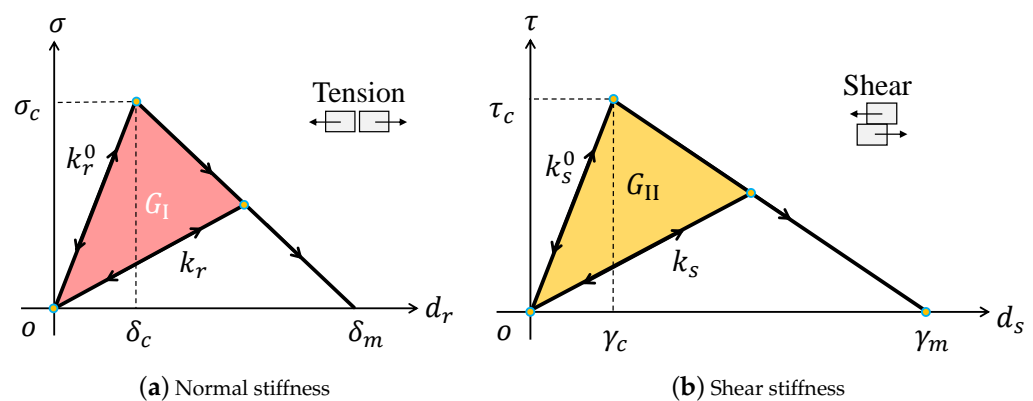

Figure 4. The bi-linear TSL relations for CS stiffness.

From Figure 4a, we can figure out k_r, i.e.,

$$k_r = \begin{cases} k_r^0, & 0 \leq d_r \leq \delta_c, \\ \dfrac{\sigma_c}{d_r} \cdot \dfrac{\delta_m - d_r}{\delta_m - \delta_c}, & \delta_c \leq d_r < \delta_m, \\ 0, & d_r \geq \delta_m. \end{cases} \tag{33}$$

From Figure 4b, k_s can be solved out as follows:

$$k_s = \begin{cases} k_s^0, & 0 \leq d_s \leq \gamma_c, \\ \dfrac{\tau_c}{d_s} \cdot \dfrac{\gamma_m - d_s}{\gamma_m - \gamma_c}, & \gamma_c \leq d_s < \gamma_m, \\ 0, & d_s \geq \gamma_m. \end{cases} \tag{34}$$

A CS fails once $d_r > \delta_m$ or $d_s > \gamma_m$, which consequently leads to a new crack between the vertexes linked by the CS. Then, the CS should be removed, and a normal contact spring should be installed along the crack surface to prevent possible interpenetration between the related adjacent sub-blocks.

In a mixed-mode fracture, both tensile and shear deformations present; the effective opening combines the individual mode separations into a single value. As illustrated in Figure 5, we adopt the following mixed-mode fracture criteria [9]:

$$\left(\frac{G_{\mathrm{I}}}{G_{\mathrm{Ic}}} \right)^2 + \left(\frac{G_{\mathrm{II}}}{G_{\mathrm{IIc}}} \right)^2 > 1. \tag{35}$$

$$G_{\mathrm{I}} = \frac{d_n - \delta_c}{\delta_m - \delta_c} G_{\mathrm{Ic}}, \qquad G_{\mathrm{II}} = \frac{d_s - \gamma_m}{\gamma_m - \gamma_c} G_{\mathrm{IIc}}. \tag{36}$$

When the inequality in Equation (35) holds, a mixed-mode fracture occurs. Then, the CS should be removed, and a normal contact spring has to be installed along the sub-block interface to prevent the possible penetration.
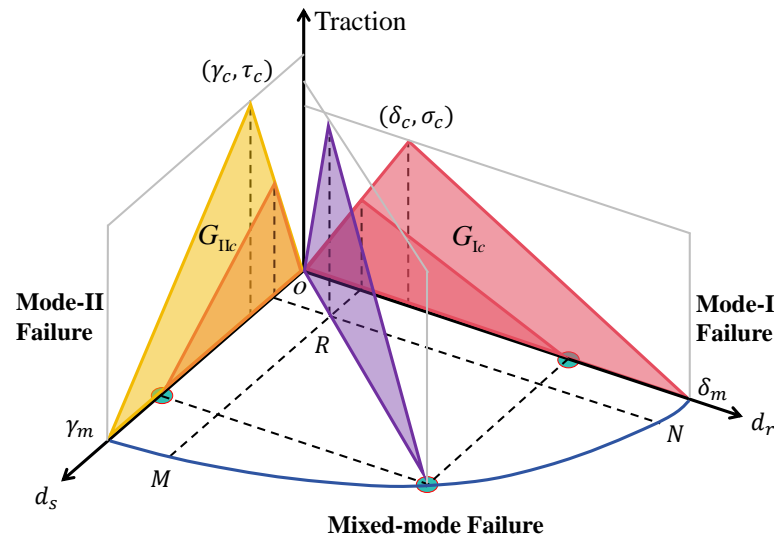

Figure 5. Mixed-mode failure criteria for CSs.

6. Implementation Aspects

The program of the proposed CDBBM method includes four main modules, as demonstrated in Figure 6.
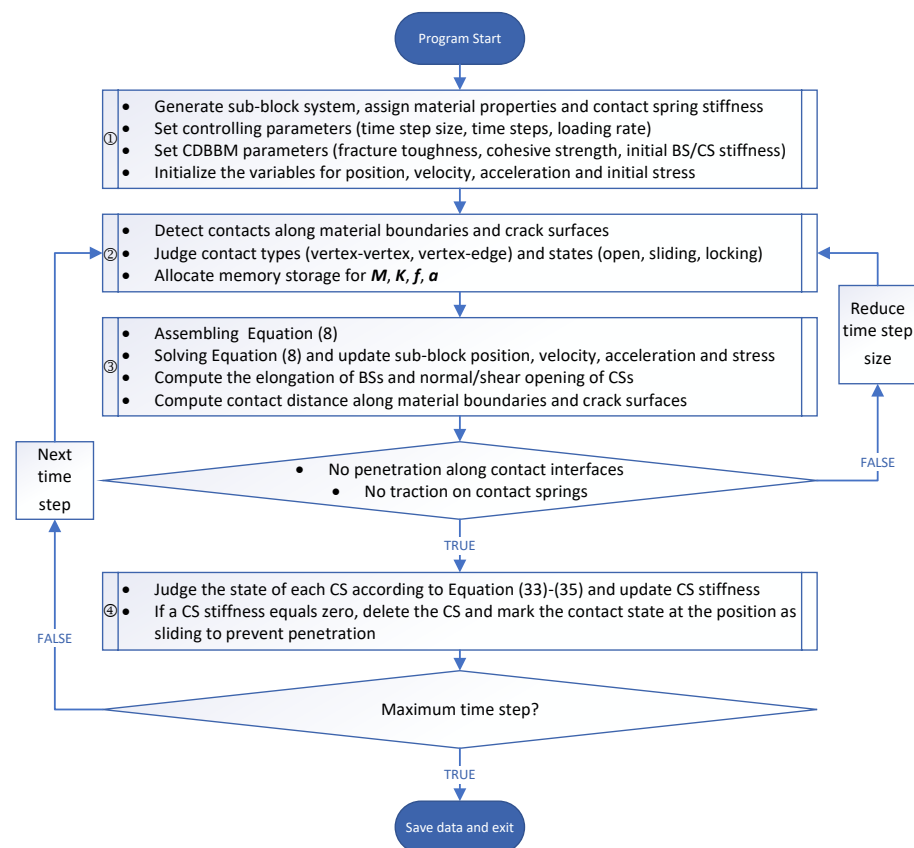

Figure 6. Flowchart of all computational modules of the CDBBM.

Module ① is responsible for data input and computation initialization. The sub-block mesh is generated from finite-element-type meshes. In the following section, we adopt quadrilateral meshes to compare the results with those obtained by the FEM [9] and the DEM [44]. The initial stiffness of each CS is determined according to Equation (32), while contact spring stiffness is usually equal to material's Young modulus. For the quadrilateral sub-block mesh, a BS's normal stiffness k_r is usually r times larger than a BS's shear stiffness k_s, where k_r varies between 100 and 200 times the Young's modulus of the material.

Module ② primarily handles contact detection, identifying both contact types and states. These contact operations follow a method similar to the traditional DDA. Notably, in the CDBBM, contacts are confined to material boundaries and crack surfaces. This approach excludes unnecessary contact operations, thereby enhancing computational efficiency.

Module ③ is used to assemble and solve Equation (3), and, afterwards, update various variables and parameters. Subsequently, the implementation of all contact springs has to be checked based on two criteria: no penetration occurring along contact interfaces and no traction being generated by contact springs. If these criteria are not met, the time step must be reduced, and the process reverts to Module 2. This iterative procedure, known as open–close iteration in the DDA, continues until the results satisfy both criteria.

In Module ④, the state of each CS is assessed using Equations (33)–(35), following which the CS stiffness is adjusted accordingly. If the CS stiffness diminishes to zero, the CS is eliminated, resulting in the vertices and edges originally linked by the CS coming into contact. At this juncture, the contact state is designated as sliding to prevent interface penetration. This designation remains in place until the subsequent open–close iteration in the subsequent time step adjusts it as needed.

7. Numerical Examples

In this section, the proposed CDBBM approach is assessed through benchmark numerical examples for continuous deformation and crack propagation problems.

7.1. Continuous Deformation

As the first numerical example, the accuracy of the CDBBM for capturing continuous deformation was validated. We consider the cantilever beam, of length $L = 30$ mm and height $h = 1$ mm, subjected to the load P at the free end, as shown in Figure 7. Young's modulus and Poisson's ratio of the beam are $E = 300$ GPa and $\nu = 0.3$, respectively. Two different quadrilateral meshes are adopted to subdivide the beam in space, as illustrated in Figure 8.
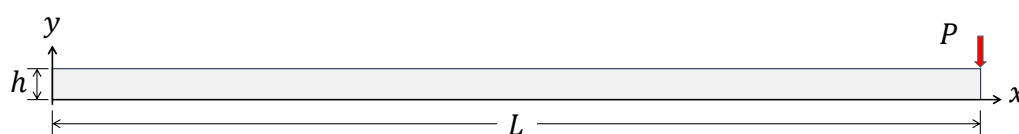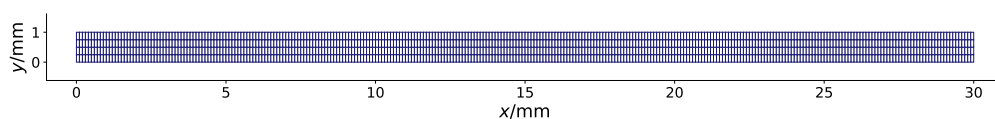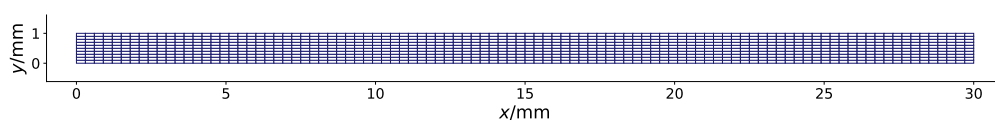

Figure 7. Geometry of the cantilever.

(**a**) Subdivision I: sub-blocks of size 0.1 mm $\times$ 0.25 mm

(**b**) Subdivision II: sub-blocks of size 0.3 mm $\times$ 0.1mm

Figure 8. Different uniform meshes for subdividing the cantilever beam as shown in Figure 7.

As shown in Figure 9, we compare the mid-plane deflection of the beam computed by the CDBBM with the analytical solution [45] given below:

$$\Delta = -\frac{Py}{6EI}\left[3\nu y^2(L-x) + \frac{4+5\nu}{4}h^2 y + (3L-x)x^2\right], \tag{37}$$

where x ranges from 0 to L, $y = h/2$, and $I = h^3/12$ is the moment of area of the beam. The comparison shows that our results using both of the two different subdivisions can provide accurate results. In the following tests, we will adopt these two spatial discretizations.

Additionally, the beam deflection computed by the original DDA is illustrated in Figure 9. Due to the use of only one block to simulate the cantilever beam in the original DDA, a disparity between the DDA result and the analytical solution can be observed. From the comparisons above, it is demonstrated that the presented CDBBM can effectively improve the deformability of blocks and shows good accordance with the analytical solution.
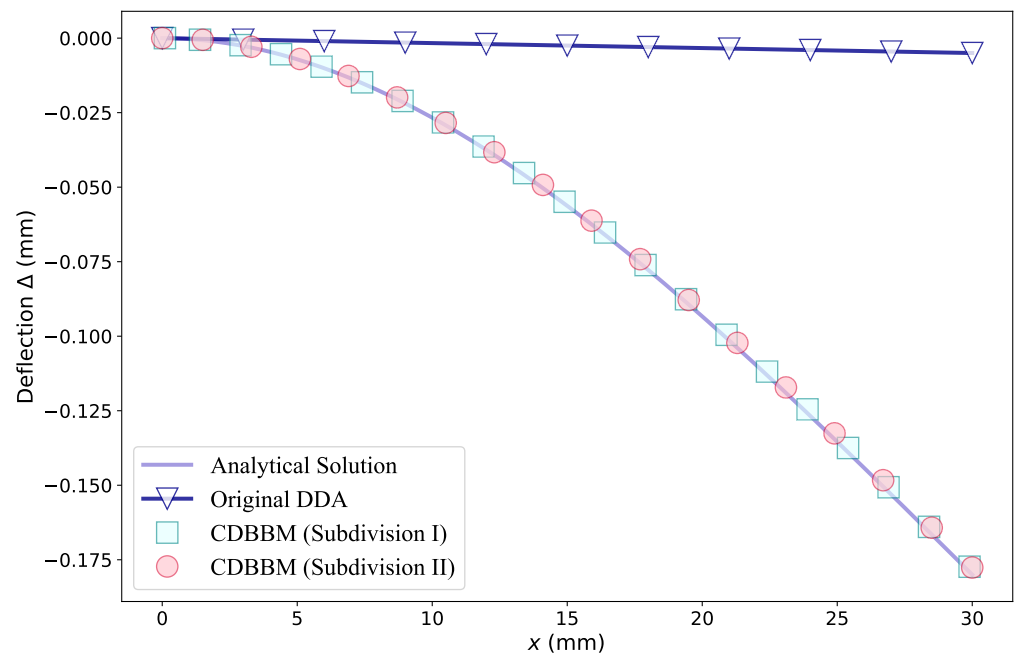

Figure 9. Comparing the result computed by the CDBBM using different spatial discretization strategies with the analytical solution and the result by the original DDA.

7.2. Mode-I Fracture

We considered the double cantilever beam (DCB), which is widely employed to characterize mode-I fracture toughness of materials. As shown in Figure 10, the specimen with the pre-crack is subjected to a pair of displacement-controlled forces. The length, half-height and the out-of-plane thickness are $2L = 30$ mm, $h = 1$ mm, and $B = 10$ mm, respectively. Moreover, the length of the pre-existing crack is $a_0 = 9$ mm. Material properties are provided in Table 1.

To numerically reproduce the fracture process of the double beam, we apply the CDBBM with the uniform quadrilateral subdivision, as shown in Figure 11. There are a total of 2400 sub-blocks of size of 0.1 mm × 0.25 mm. Under the loading rate $v = 0.001$ mm/ms, we illustrate the snapshot of the deformed specimen at $t = 1200$ ms, as shown in Figure 12. Our result is accordance with the simulations presented by the FEM [9] and the DEM [44].

Table 1. Material parameter settings for the DCB, ENF, and MMB tests.

Parameters (Unit)	DCB	ENF	MMB
E (GPa)	126	70	70
ν	0.2	0.25	0.25
G_{Ic} (MPa)	0.13/0.26/0.39	0.26	1.002
G_{IIc} (MPa)	1.002	1.002	1.002
σ_c (MPa)	35/70/105	70	4/7
τ_c (MPa)	200	200/220/240	4/7/10
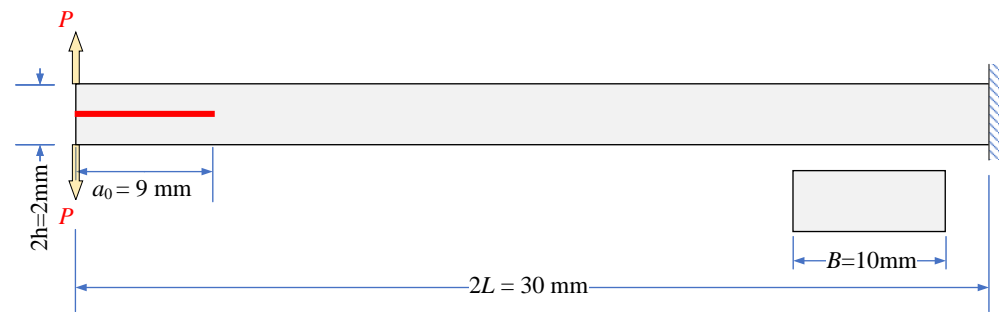
Figure 10. Geometry configuration for the specimen used in the DCB test.
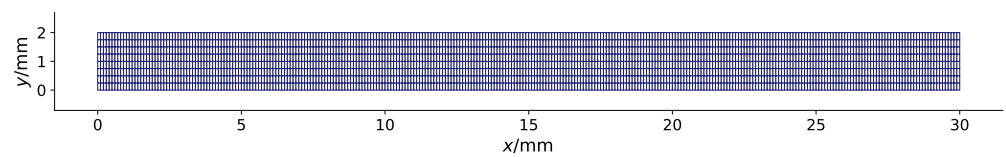
Figure 11. The subdivision adopted by the CDBBM for the DCB test.

(**a**) σ_x (MPa)

(**b**) σ_y (MPa)
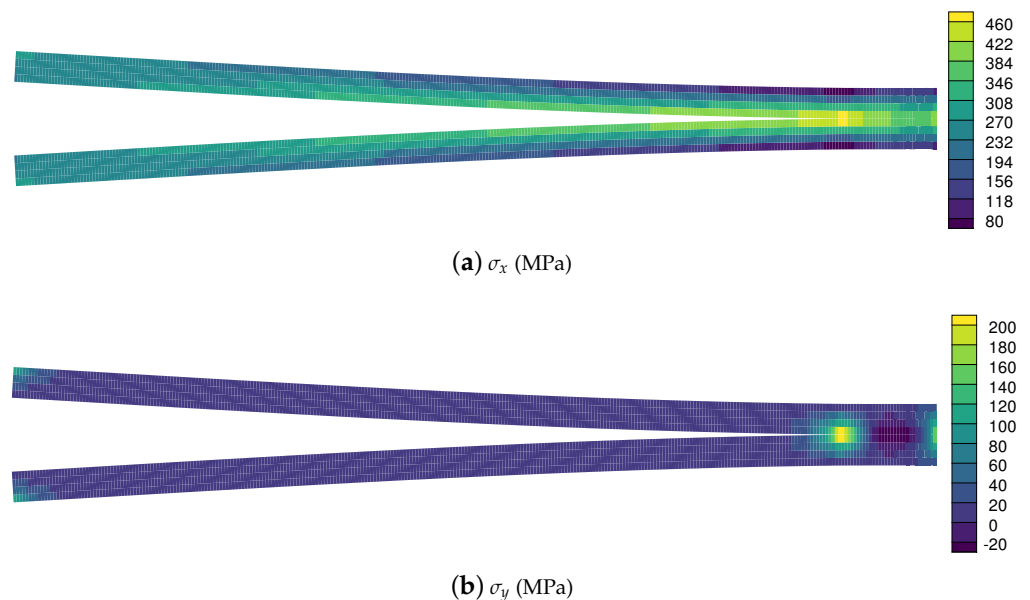
Figure 12. The results computed by the CDBBM with the loading rate $v = 0.001$ mm/ms at $t = 1200$ ms for the DCB test.

Below, we compare the numerical results obtained from the CDBBM with analytical solutions to validate the accuracy of our method. The comparisons were conducted under various conditions, including different loading rates v, different critical stresses σ_c, and different mode-I fracture toughness values G_{Ic}. The analytical solution [44] for the DCB test

describes the variation of the traction P as the deflection Δ at the free end increases. We use a to denote the crack length, and the analytical solution can be expressed as follows:

$$\Delta_{OA} = \frac{2P(a_0 + \chi_I h)^3}{3EI}, \quad a = a_0, \tag{38}$$

$$\Delta_{BCD} = \frac{2P(BEIG_{\text{Ic}})^{3/2}}{3EI}, \quad a_0 < a < 2L, \tag{39}$$

$$\Delta_{OE} = \frac{Py}{6EI}\left[3vy^2(L-x) + \frac{1}{4}(4+5v)h^2y + (3L-x)x^2\right], \quad a = 2L, \tag{40}$$

where I is the moment of area of one arm, $(x, y) = (0, h)$, and χ_I is the correction factor, i.e.,

$$I = \frac{Bh^3}{12}, \quad \chi_I = \sqrt{\frac{E}{11G}\left(3 - 2\left(\frac{\Gamma}{1+\Gamma}\right)^2\right)}, \tag{41}$$

in which $\Gamma = 1.18E/G$ is the correction coefficient. The analytical solution is plotted as shown in Figure 13, where the curves OA, BCD, and OE correspond to Equation (38), Equation (39), and Equation (40), respectively.

Firstly, we investigated the effect of the traction P at different loading rates, including the low rate $v = 5 \times 10^{-4}$ mm/ms, the medium rate $v = 1 \times 10^{-3}$ mm/ms, and the high rate $v = 2 \times 10^{-3}$ mm/ms. From Figure 13, we can observe that the numerical result using the medium loading rate closely match the analytical solutions, indicating an accurate crack propagation prediction by the CDBBM. In contrast, both low and high loading rates lead to slight deviations from the analytical solution, which can be attributed to the dynamic effects becoming more pronounced. The observed phenomena are consistent with the results presented in Xie and Waas's work [9].
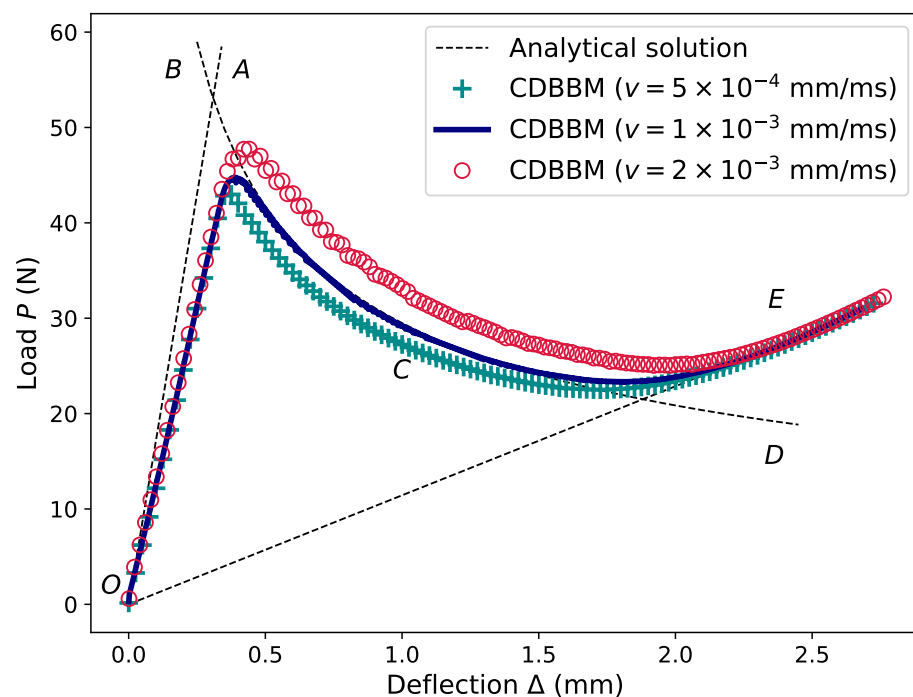

Figure 13. Results compared to analytical solutions with different loading rates v.

Secondly, we examined the influence of cohesive strength on crack behavior at a constant loading rate of $v = 0.001$ mm/ms. Figure 14 presents three load-deflection curves corresponding to low cohesive strength ($\sigma_c = 35$ MPa), medium cohesive strength

($\sigma_c = 70$ MPa), and high cohesive strength ($\sigma_c = 105$ MPa). All results demonstrate good agreement with the analytical solution. Notably, cohesive strength does not appear in Equations (38)–(40). However, the figure indicates that crack propagation becomes slightly more difficult as the cohesive strength increases. These findings are consistent with the relationship demonstrated in Figure 4, where a bigger σ_c means a larger critical opening δ_c and a smaller maximum opening δ_m. In Table 2, the load P for different opening values computed by the CDBBM is demonstrated against the analytical solutions. The accuracy of our method is evidenced by the satisfactory relative errors presented.
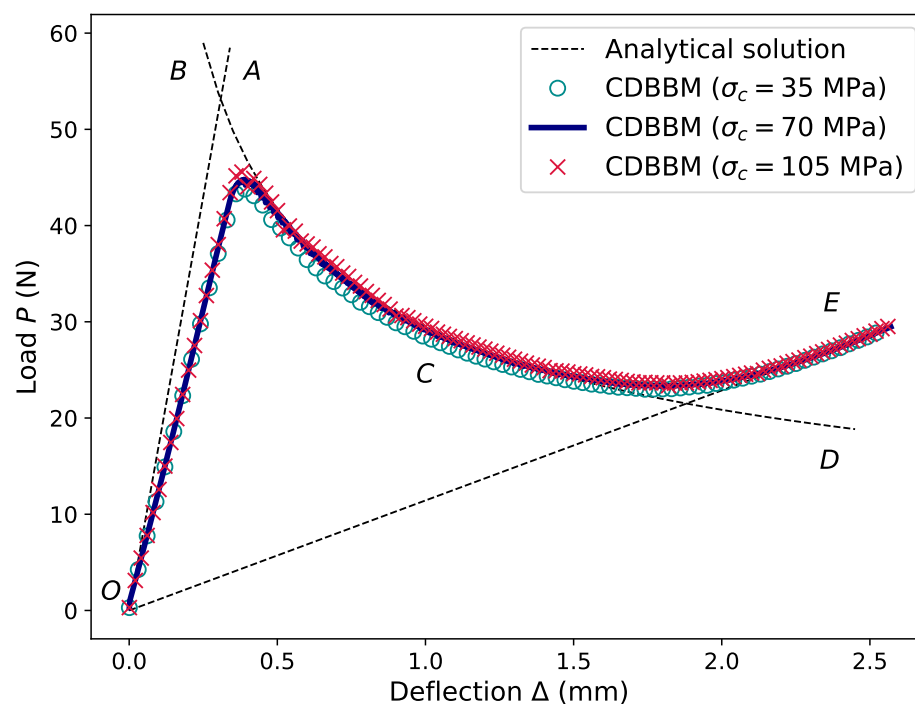

Figure 14. Results compared to analytical solutions with different critical stresses σ_c.

Thirdly, we studied the impact of varying mode-I fracture toughness values on the numerical results by conducting the simulations with low fracture toughness ($G_{\text{Ic}} = 0.13$ N/mm), medium fracture toughness ($G_{\text{Ic}} = 0.13$ N/mm), and high fracture toughness ($G_{\text{Ic}} = 0.13$ N/mm). As illustrated in Figure 15, our results for both low and medium fracture toughness agree with the analytical solution very well. Specifically, the crack propagates quickly when using low fracture toughness, while the crack has moderate propagation rates when adopting medium fracture toughness. However, the crack propagation is significantly slower in the case of high fracture toughness, and the numerical results deviate slightly from the analytical solution.

Table 2. The load P computed by the CDBBM for different normal openings Δ against the analytical solutions using diverse cohesive strengths σ_c for the DCB test with the constant loading rate $v = 0.001$ mm/ms.

| Δ (mm)	Exact (N)	$\sigma_c = 35$ MPa		$\sigma_c = 75$ MPa		$\sigma_c = 105$ MPa	
		Numerical	Error	Numerical	Error	Numerical	Error
0.50	41.708328	40.145871	3.75×10^{-2}	41.405462	7.26×10^{-3}	41.551019	3.77×10^{-3}
0.75	34.054707	32.809289	3.66×10^{-2}	33.825025	6.74×10^{-3}	34.429044	1.10×10^{-2}
1.00	29.492242	28.425323	3.62×10^{-2}	29.202222	9.83×10^{-3}	29.533051	1.38×10^{-3}
1.25	26.378663	25.654516	2.75×10^{-2}	26.270182	4.11×10^{-3}	26.629217	9.50×10^{-3}
1.50	24.080314	23.815309	1.10×10^{-2}	24.305141	9.34×10^{-3}	24.601673	2.17×10^{-2}
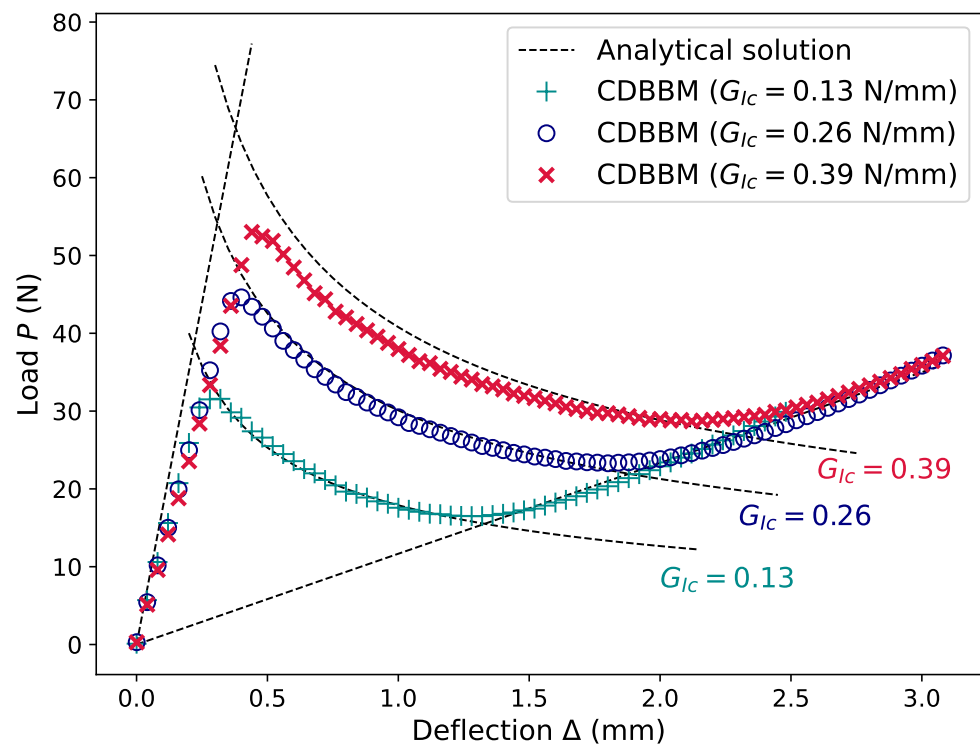
Figure 15. Results compared to analytical solutions with different fracture toughnesses G_{Ic}.

7.3. Mode-II Fracture

Next, the end-notched flexural (ENF) problem was considered. The ENF test is a critical experiment for understanding the shear-driven crack propagation in materials and provides valuable insights into the mode-II fracture toughness, which is essential for designing materials that can withstand shear loads without catastrophic failure. As shown in Figure 16, the specimen with a prescribed crack is subjected to a displacement-controlled shearing force acting at the mid-span of the specimen. In this test, we set the loading rate $v = 0.001$ mm/s. Furthermore, the material constants are supplied in Table 1.
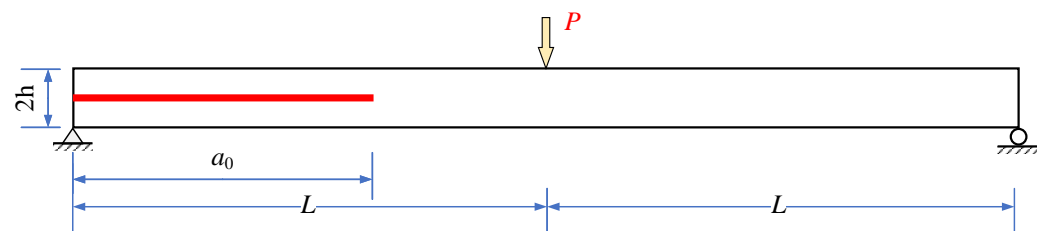

Figure 16. The geometry configuration for the ENF test: the length $2L = 30.3$ mm, the half-height $h = 1$ mm, the out-of-plane thickness $B = 3$ mm, and the length of pre-existing crack $a_0 = 9$ mm.

To simulate the ENF test, we employed the CDBBM with the quadrilateral subdivision as illustrated in Figure 17, where each sub-block is 0.3 mm in width and 0.1 mm in height. In the case of using the critical shear strength $\tau_c = 220$ MPa, we obtained the deformation and stress results at $t = 1800$ ms, as illustrated in Figure 18. The contact effect along the interface between the separated arms can be observed. Our results are consistent with the simulations presented in existing studies [9,44].
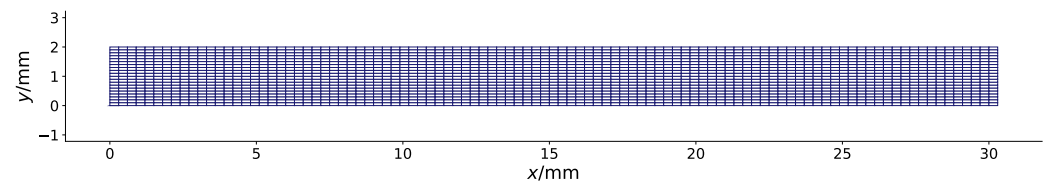
Figure 17. The uniform quadrilateral sub-block mesh for the ENF test.

Below, the results from this numerical experiment are compared with analytical solutions to validate the accuracy and reliability of our method. Mi et al. [46] provided the analytical solution for the ENF test as follows:

$$\Delta_{OB} = \frac{P(2L^2 + 3a^3)}{96EI}, \quad a = a_0, \tag{42}$$

$$\Delta_{BCD} = \frac{P}{96EI}\left[2L^3 + \frac{(64G_{IIc}BEI)^{3/2}}{\sqrt{3}P3}\right], \quad a_0 < a \leq L, \tag{43}$$

$$\Delta_{EF} = \frac{P}{24EI}\left[2L^3 - \frac{(64G_{IIc}BEI)^{3/2}}{4\sqrt{3}P3}\right], \quad L < a < 2L, \tag{44}$$

$$\Delta_{OG} = \frac{PL^3}{12EI}, \quad a = 2L, \tag{45}$$

where a tracks the length of the crack. As shown in Figure 19, the deflection–load curves, i.e., OB, BCD, EF, and OG, represent Equations (42)–(45), respectively.

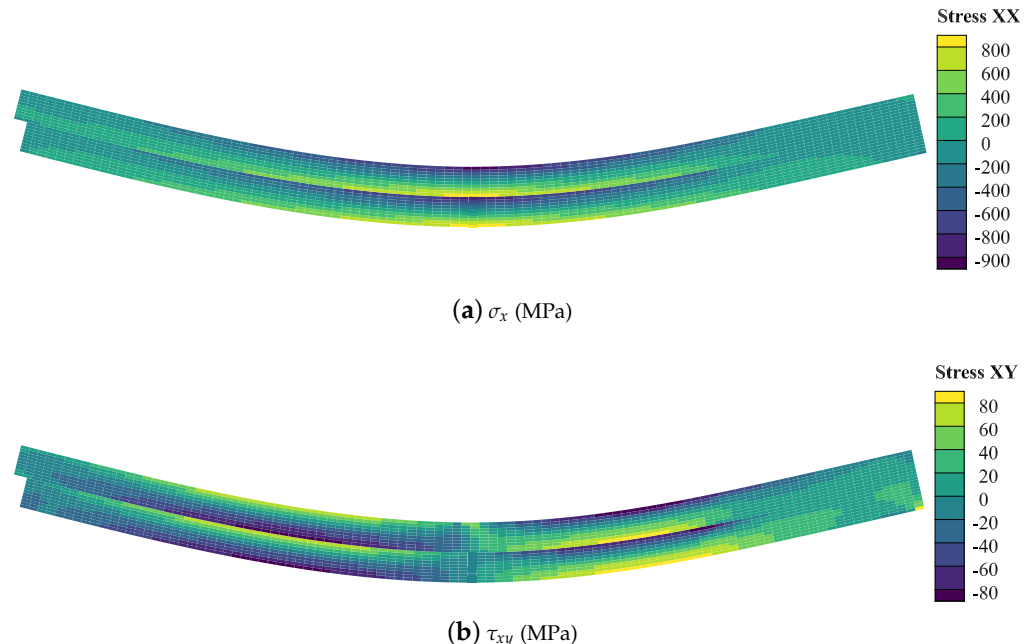(**a**) σ_x (MPa)

(**b**) τ_{xy} (MPa)

Figure 18. The results computed by the CDBBM for the ENF test with $\tau_c = 220$ MPa at $t = 1800$ ms.

Here, we investigated the effect of different critical shear cohesive strengths, i.e., low strength ($\tau_c = 150$ MPa), medium strength ($\tau_c = 180$ MPa), and high strength ($\tau_c = 210$ MPa). As shown in Figure 19, the result computed by the CDBBM agrees with the analytical solution very well for the medium strength. Furthermore, we can observe that higher shear cohesive strengths possess a faster crack propagation rate. This behavior aligns with the relation given in Figure 4. Furthermore, it is worth noting that our results deviate slightly from the analytical curve OG. Such a deviation is due to our method accounting for the

contact interaction between the separated arms, whereas the analytical solution is just based on beam theory. Our simulations are consistent with the results presented by Xie and Waas [9] and the references therein.
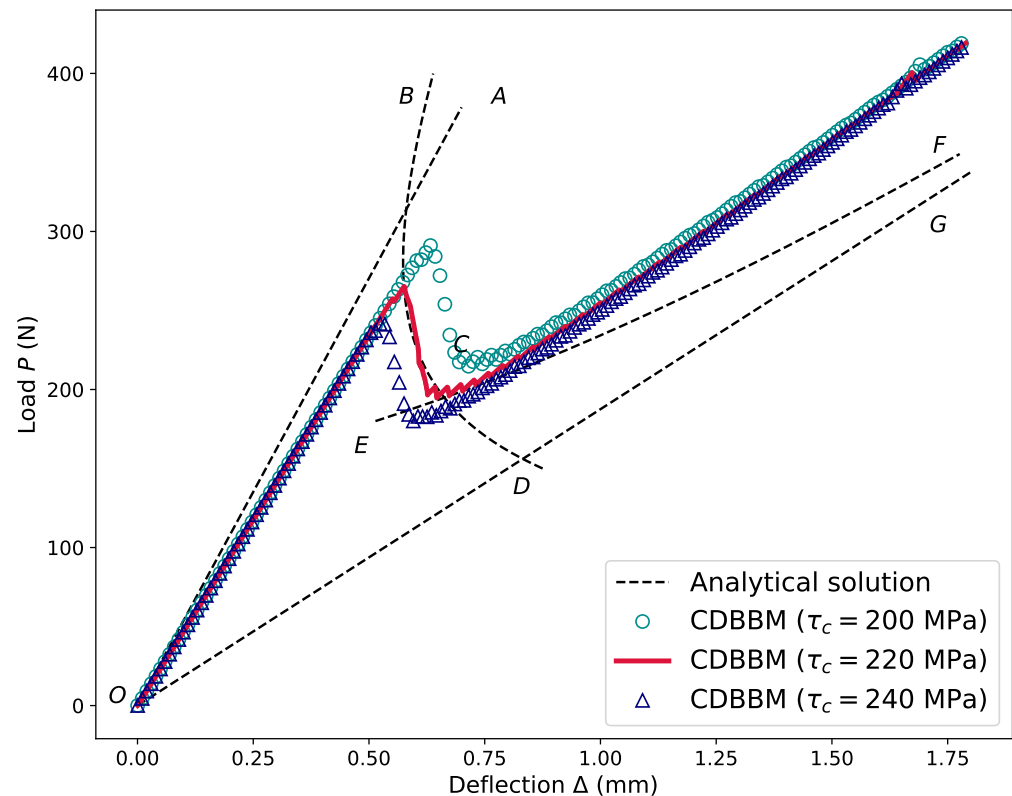

Figure 19. Results compared with analytical solution for the ENF test using different critical stresses.

7.4. Mixed-Mode Fracture

In this section, the mixed-mode bending (MMB) problem is considered, with the specimen geometry illustrated in Figure 20. A long lever with two vertical legs is placed above the beam to supply the displacement-controlled loading at a rate of $P = 0.001$ mm/ms. One leg of the lever is fixed at the beam's left end, while the other leg contacts the beam at its midpoint on the top surface. The specimen's material parameters are offered in Table 1. Furthermore, we set the lever's Young modulus at $E_0 = 700$ GPa and Poisson's ratio at $v_0 = 0.3$.

The proposed CDBBM method was used to simulate the MMB problem with the uniform quadrilateral mesh as shown in Figure 21. Each sub-block's width is 0.1 mm and its height is 0.25 mm. The horizontal arm and the two legs of the lever are each simulated by three intact blocks, with the two legs glued to the bottom of the horizontal arm by bonding springs. Figure 22 illustrates the simulation results for the normal cohesive strength $\sigma_c = 4$ MPa and the shear cohesive strength $\tau_c = 7$ MPa at $t = 2500$ ms. The predictions for the deformation and stress distribution align with the simulations conducted by the FEM [9] and the DEM [44].
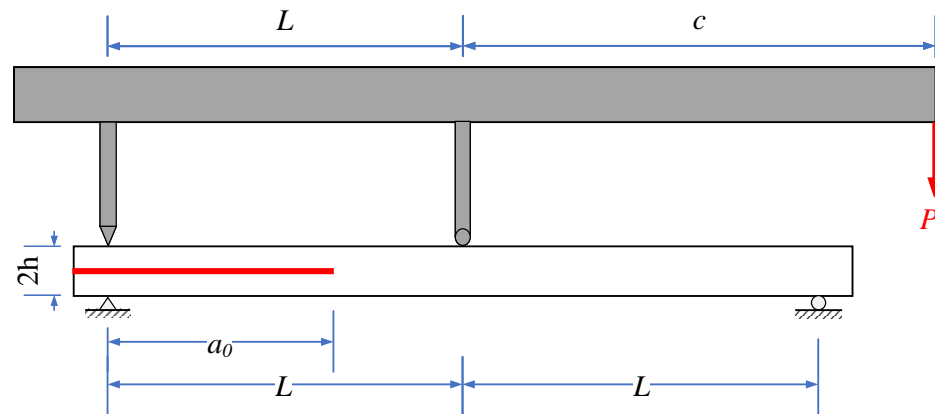
Figure 20. Geometry configuration of the MMB test. The specimen has a length of $2L = 30$ mm, the half-height $h = 1$ mm, the out-of-plane thickness $B = 5$ mm, and the pre-existing crack length $a_0 = 9$ mm. The long lever above the specimen has the size parameters $c = 13.1$ mm.
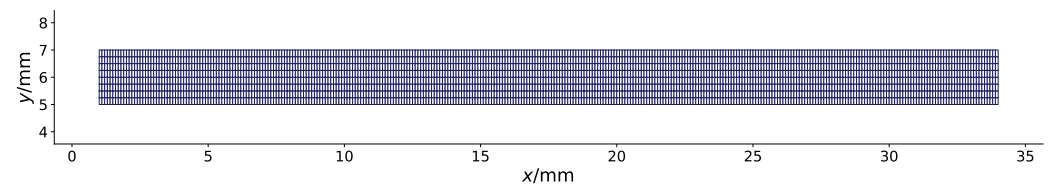

Figure 21. The uniform quadrilateral sub-block mesh for the MMB test. A total of 3310 quadrilateral sub-blocks are employed.

(a) σ_x (MPa)

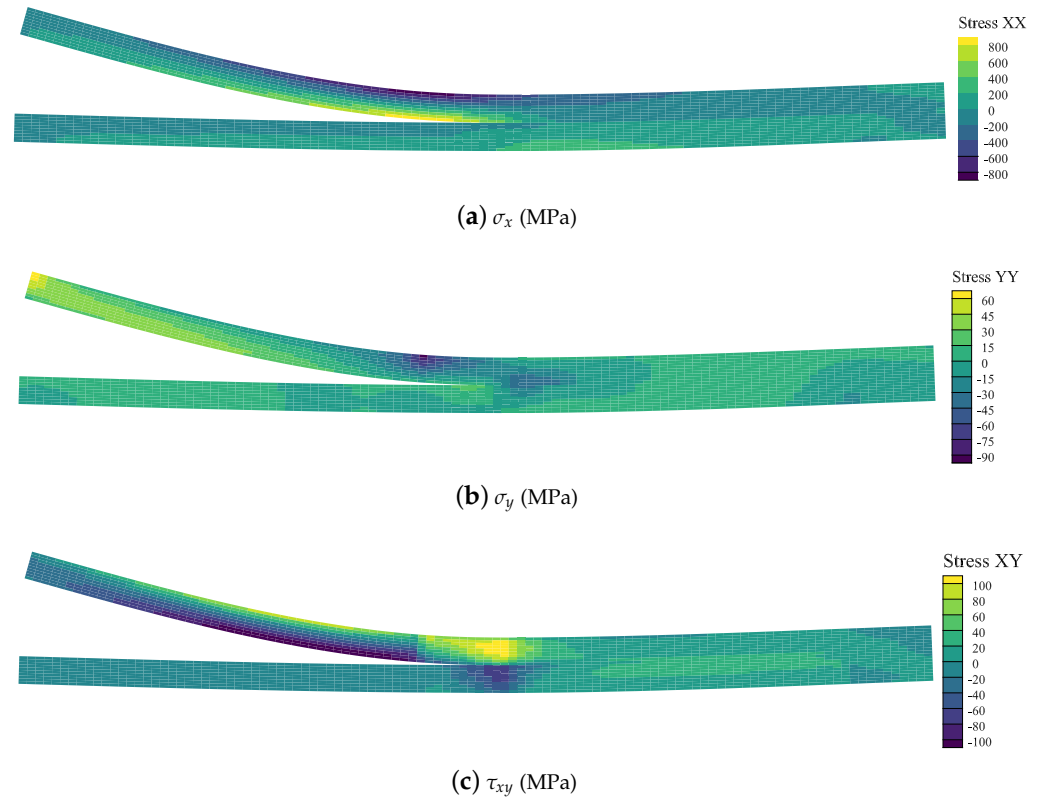**(b)** σ_y (MPa)

(c) τ_{xy} (MPa)

Figure 22. The deformation and stress distribution computed by the improved SDDA approach in the MMB test with the loading rate $v = 0.001$ mm/ms at $t = 2500$ ms.

For this test, Mi et al. [46] have supplied the analytical solution for the deflection–load relation according to the varying crack length a, i.e.,

$$\Delta_{OA} = \frac{2}{3}\left(\frac{3c - L}{4L}\right)\frac{Pa_0^3}{EI}, \quad a = a_0, \tag{46}$$

$$\Delta_{BCD} = \frac{2P_I}{3EI}\left(\frac{8BEI}{\frac{8P_I^2}{G_{Ic}} + \frac{3P_{II}^2}{8G_{IIc}}}\right)^{3/2}, \quad a_0 < a \le L, \tag{47}$$

$$\Delta_{EF} = \frac{2}{3}\left(\frac{3c - L}{4L}\right)\frac{Pa^3}{EI}, \quad a > L, \tag{48}$$

where the mode-I load P_I and the mode-II load P_{II} take the following formulas:

$$P_I = \left(\frac{3c - L}{4L}\right)P, \qquad P_{II} = \left(\frac{c + L}{L}\right)P. \tag{49}$$

In Equation (48), the crack length a is the solution of the equation below:

$$\alpha\left(\frac{8P_I^2}{G_{Ic}} + \frac{3P_{II}^2}{8G_{IIc}} - \frac{8P_I P_{II}}{G_{IIc}}\right)a^2 - \frac{L\alpha}{G_{IIc}}\left(\frac{3P_{II}^2 L}{2} - 8P_I P_{II}\right)a + \frac{3P_{II}^2 L^2 \alpha}{2G_{IIc}} - 1 = 0, \tag{50}$$

where $\alpha = \frac{1}{8BEI}$. As shown in Figure 23, we illustrate the deflection–load curves OA, BCD, and EF for Equation (46), Equation (47), and Equation (48), respectively.

Below, we examine the influence of σ_c and τ_c on the crack propagation process.
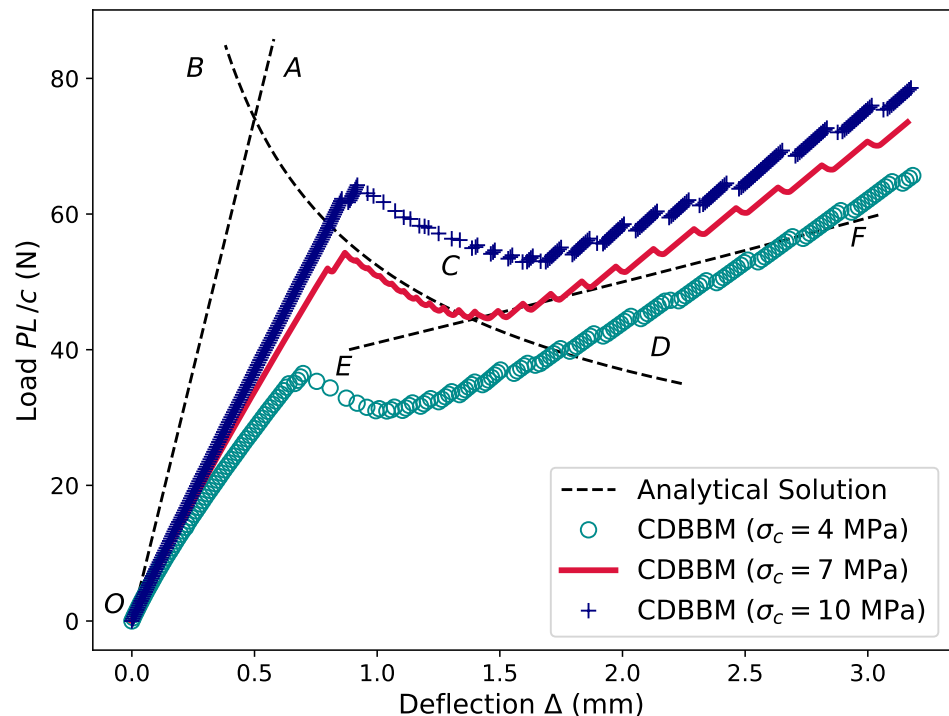

Figure 23. CDBBM simulation results against the analytical solution for the MMB test with varying normal cohesive strengths $\sigma_c = 4, 7$, and 10 MPa and the shear cohesive strength $\tau_c = 7$ MPa.

To investigate the effect of normal cohesive strength, we adopted the shear cohesive strength $\tau_c = 7$ MPa, and used three different normal cohesive strengths, i.e., low normal strength ($\tau_c = 4$ MPa), medium normal strength ($\tau_c = 7$ MPa), and high normal strength ($\tau_c = 10$ MPa). As shown in Figure 23, the results obtained by our method are compared

with the analytical solution. It is evident that the CDBBM method accurately captures the overall trend of the load-deflection behavior, as predicted by the analytical curves as well as the simulations presented in the literature [9]. For the low normal cohesive strength $\sigma_c = 4$, the computing results slightly underestimate the peak load, while the CDBBM results can better approximate the peak load as σ_c increases to 7 MPa. When σ_c increases to 10 MPa, the crack propagation rate is slower than the cases of smaller normal cohesive strengths. It should be noted that our simulation deviates slightly from the analytical solution, i.e., the curve *EF*, during the post-peak stage. This discrepancy reveals the influence of the crack closure effect along the interface of the separated arms.

Then, we used the normal cohesive strength $\sigma_c = 7$ MPa and adopted varying shear cohesive strengths, i.e., low shear strength ($\tau_c = 4$ MPa), medium shear strength ($\tau_c = 7$ MPa), and high shear strength ($\tau_c = 10$ MPa). Figure 24 compares the results against the analytical solution. The comparison shows that our results align with the analytical curve very well. Additionally, we can also notice that a lower shear cohesive strength leads to a slight derivation from the critical loading and a faster crack propagation rate.
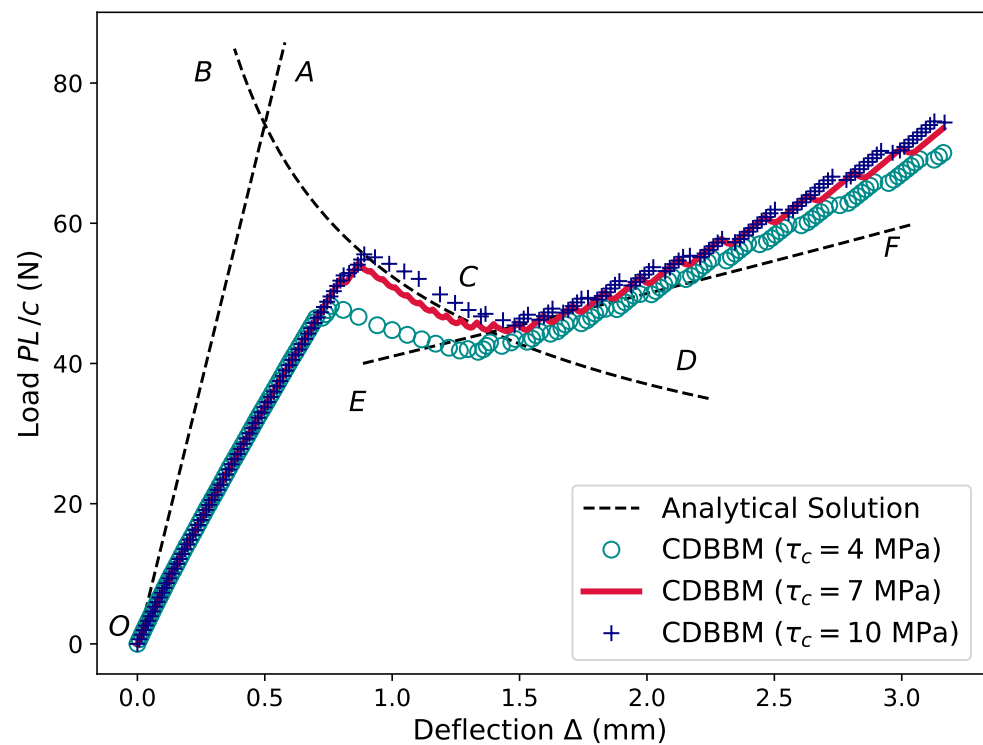

Figure 24. CDBBM simulation results against the analytical solution for the MMB test with the normal cohesive strength $\sigma_c = 7$ MPa and the varying shear cohesive strengths $\tau_c = 4, 7$, and 10 MPa.

8. Conclusions

In this paper, a continuum–discontinuum bonded-block model (CDBBM) was developed for simulating mixed-mode fracture of quasi-brittle solids. The CDBBM enriches the DDA with the partitioning of material into a continuum region and a potential discontinuum region, employing bonding springs (BSs) and cohesive springs (CSs) to glue the sub-blocks within the two regions, respectively. Diversified benchmark numerical experiments were conducted to examine the proposed method for modeling continuous deformation, pure mode-I/-II and mixed-mode fractures. From the simulation results and the comparisons against analytical solutions, a few attractive features of the CDBBM can be outlined:

(1) By adopting specialized modeling techniques for both continuum and potential discontinuum regions, the CDBBM can accurately and effectively predict both continuous

deformation and material failure. Additionally, utilizing an implicit time integration scheme ensures highly stable computation results, even when using large time steps.

(2) Material continuity is maintained by the BSs and CSs along adjacent sub-block interfaces, confining contact interactions to the discontinuities within the material. This approach allows the CDBBM to achieve high computational efficiency by avoiding complex contact operations, such as determining contact types and states, transferring parameters between steps, and repeatedly assembling contact sub-matrices.

(3) In the CDBBM, the transition of material from a continuous to a discontinuous stage is effectively modeled by the degradation of CSs. This degradation process accurately represents material failure, ensuring stability and consistency along uncracked interfaces. By avoiding the need for frequent mesh updates typically required in cohesive element approaches, the CDBBM maintains correct contact simulation across closed crack surfaces, thus circumventing common issues such as mesh distortion and maintaining the integrity of the simulation throughout the fracture process.

(4) The numerical simulation results presented in Section 7 showcase the versatility and robustness of the CDBBM. The method accurately simulates mode-I, mode-II, and mixed-mode cracks through various benchmark numerical examples, demonstrating its broad applicability. By effectively managing the complexities inherent in mixed-mode fractures, the CDBBM accurately captures the interactions between tensile and shear components.

The merits outlined above underscore the method as a powerful tool for capturing the interplay between continuum deformation, crack initiation, and fracture propagation. This makes it highly applicable for reliably modeling complex fracture behaviors across diverse engineering applications. However, it should be acknowledged that our research findings are still in their initial stages. For instance, while our proposed method shows promise and potential for application in multi-crack growth simulations, this has not yet been explored in the current study. We are committed to addressing these challenges in our ongoing research and look forward to advancing our method in these areas.

Author Contributions: Conceptualization, methodology and software, Y.S.; validation, T.C.; visualization, L.Y.; original draft preparation, Q.C. All authors have read and agreed to the published version of the manuscript.

Data Availability Statement: The original contributions presented in the study are included in the article, further inquiries can be directed to the corresponding author.

Conflicts of Interest: The authors declare no conflicts of interest.

References

1. Kinloch, A.J.; Wang, Y.; Williams, J.G.; Yayla, P. The mixed-mode delamination of fibre composite materials. *Compos. Sci. Technol.* **1993**, *47*, 225–237. [CrossRef]
2. Allix, O.; Ladevéze, P.; Corigliano, A. Damage analysis of interlaminar fracture specimens. *Compos. Struct.* **1995**, *31*, 61–74. [CrossRef]
3. Goyal, V.K. Analytical Modeling of the Mechanics of Nucleation and Growth of Cracks. Ph.D. Thesis, VirginiaPolytechnic Institute and State University, Blacksburg, VA, USA, 2002.
4. Azab, M.; Parry, G.; Estevez, R. An analytical model for DCB/wedge tests based on Timoshenko beam kinematics for accurate determination of cohesive zone lengths. *Int. J. Fract.* **2020**, *222*, 137–153. [CrossRef]
5. Reeder, J.R.; Crews, J.H. Mixed-Mode Bending Method for Delamination Testing. *AIAA J.* **1990**, *28*, 1270–1276. [CrossRef]
6. Jia, M.; Wu, Z.; Yu, R.C.; Zhang, X. Experimental investigation of mixed mode I–II fatigue crack propagation in concrete using a digital image correlation method. *Eng. Fract. Mech.* **2022**, *272*, 108712. [CrossRef]
7. Xie, Q.; Qi, H.; Li, S.; Yang, X.; Shi, D. Experimental and numerical investigation of mixed-mode fatigue crack growth in nickel-based superalloy at high temperature. *Eng. Fract. Mech.* **2022**, *273*, 108736. [CrossRef]
8. Camanho, P.P.; Davila, C.G.; De Moura, M.F. Numerical Simulation of Mixed-Mode Progressive Delamination in Composite Materials. *J. Compos. Mater.* **2003**, *37*, 1415–1438. [CrossRef]

9.   Xie, D.; Waas, A.M. Discrete cohesive zone model for mixed-mode fracture using finite element analysis. *Eng. Fract. Mech.* **2006**, *73*, 1783–1796. [CrossRef]

10. Camanho, P.; Bessa, M.; Catalanotti, G.; Vogler, M.; Rolfes, R. Modeling the inelastic deformation and fracture of polymer composites—Part II: Smeared crack model. *Mech. Mater.* **2013**, *59*, 36–49. [CrossRef]

11. Belnoue, J.P.H.; Hallett, S.R. Cohesive/adhesive failure interaction in ductile adhesive joints Part I: A smeared-crack model for cohesive failure. *Int. J. Adhes. Adhes.* **2016**, *68*, 359–368. [CrossRef]

12. Saikia, P.; Muthu, N. Extrinsic cohesive zone modeling for interface crack growth: Numerical and experimental studies. *Eng. Fract. Mech.* **2022**, *266*, 108353. [CrossRef]

13. Tang, C.; Tang, S.; Gong, B.; Bai, H. Discontinuous deformation and displacement analysis: From continuous to discontinuous. *Sci. China Technol. Sci.* **2015**, *58*, 1567–1574. [CrossRef]

14. Bolander, J.E.; Eliáš, J.; Cusatis, G.; Nagai, K. Discrete mechanical models of concrete fracture. *Eng. Fract. Mech.* **2021**, *257*, 108030. [CrossRef]

15. Gee, B.; Parchei-Esfahani, M.; Gracie, R. XFEM simulation of a mixed-mode fracture experiment in PMMA. *Eng. Fract. Mech.* **2020**, *229*, 106945. [CrossRef]

16. Mehraban, M.R.; Bahrami, B.; Ayatollahi, M.; Nejati, M. A non-local XFEM-based methodology for modeling mixed-mode fracturing of anisotropic rocks. *Rock Mech. Rock Eng.* **2023**, *56*, 895–909. [CrossRef]

17. Yang, L.; Yang, Y.; Zheng, H. A phase field numerical manifold method for crack propagation in quasi-brittle materials. *Eng. Fract. Mech.* **2021**, *241*, 107427. [CrossRef]

18. Liu, Z.; Jiang, Y.; Yang, H.; Cai, Z.; Tong, Y.; Zhang, F. Preconditioned numerical manifold method for linear elastic fractures. *Comput. Methods Appl. Mech. Eng.* **2023**, *406*, 115911. [CrossRef]

19. Shi, G.H. Discontinuous Deformation Analysis: A New Numerical Model for the Statics and Dynamics of Block Systems. Ph.D. Thesis, University of California, Berkeley, CA, USA, 1988.

20. Jiao, Y.Y.; Zhao, Q.; Zheng, F.; Wang, L. Latest advances in discontinuous deformation analysis method. *Sci. China Technol. Sci.* **2017**, *60*, 963–964. [CrossRef]

21. Potyondy, D.O.; Cundall, P. A bonded-particle model for rock. *Int. J. Rock Mech. Min. Sci.* **2004**, *41*, 1329–1364. [CrossRef]

22. Zhao, J.; Sun, W.; Luo, H.; Wu, S.; Hou, Z. Effect of thermal treatment on microcracking characteristics of granite under tensile condition based on bonded-particle model and moment tensor. *Sci. Rep.* **2024**, *14*, 8806. [CrossRef] [PubMed]

23. Inga, C.E.C.; Sinha, S.; Walton, G.; Holley, E. Modeling Brazilian tensile strength tests on a brittle rock using deterministic, semi-deterministic, and Voronoi bonded block models. *Rock Mech. Rock Eng.* **2023**, *56*, 5293–5313. [CrossRef]

24. Lemos, J.V. Application of Bonded-Block Models to Rock Failure Analysis. *Appl. Sci.* **2023**, *13*, 12207. [CrossRef]

25. Ni, K.; Yang, J.; Ning, Y.; Kang, G. A modified sub-block DDA fracturing modelling method for rock. *Eng. Anal. Bound. Elem.* **2020**, *111*, 154–166. [CrossRef]

26. Jiao, Y.Y.; Zhang, X.L.; Zhao, J. Two-Dimensional DDA Contact Constitutive Model for Simulating Rock Fragmentation. *J. Eng. Mech.* **2011**, *138*, 199–209. [CrossRef]

27. Hu, C.; Gong, S.; Zhuang, D.; Ling, D.; Wei, G.; Chen, G. Improved discontinuous deformation analysis method for modeling tensile cracking in quasi-brittle materials. *Theor. Appl. Fract. Mech.* **2023**, *124*, 103748. [CrossRef]

28. Zhang, Y.; Wang, J.; Zhao, J.X.; Chen, G.; Yu, P.; Yang, T. Multi-spring edge-to-edge contact model for discontinuous deformation analysis and its application to the tensile failure behavior of rock joints. *Rock Mech. Rock Eng.* **2020**, *53*, 1243–1257. [CrossRef]

29. Yu, P.; Zhang, Y.; Peng, X.; Chen, G.; Zhao, J.X. Distributed-Spring Edge-to-Edge Contact Model for Two-Dimensional Discontinuous Deformation Analysis. *Rock Mech. Rock Eng.* **2020**, *53*, 365–382. [CrossRef]

30. Zheng, F.; Zhuang, X.; Zheng, H.; Jiao, Y.Y.; Rabczuk, T. Discontinuous deformation analysis with distributed bond for the modelling of rock deformation and failure. *Comput. Geotech.* **2021**, *139*, 104413. [CrossRef]

31. Chang, X.; Hu, C.; Zhou, W.; Ma, G.; Zhang, C. A combined continuous-discontinuous approach for failure process of quasi-brittle materials. *Sci. China Technol. Sci.* **2014**, *57*, 550–559. [CrossRef]

32. Gui, Y.L.; Bui, H.H.; Kodikara, J.; Zhang, Q.B.; Zhao, J.; Rabczuk, T. Modelling the dynamic failure of brittle rocks using a hybrid continuum-discrete element method with a mixed-mode cohesive fracture model. *Int. J. Impact Eng.* **2016**, *87*, 146–155. [CrossRef]

33. Yan, C.; Zheng, H.; Sun, G.; Ge, X. Combined finite-discrete element method for simulation of hydraulic fracturing. *Rock Mech. Rock Eng.* **2016**, *49*, 1389–1410. [CrossRef]

34. Xu, W.; Zang, M.; Sakamoto, J. Modeling mixed mode fracture of concrete by using the combined discrete and finite elements method. *Int. J. Comput. Methods* **2016**, *13*, 1650007. [CrossRef]

35. Fukuda, D.; Liu, H.; Zhang, Q.; Zhao, J.; Kodama, J.I.; Fujii, Y.; Chan, A.H.C. Modelling of dynamic rock fracture process using the finite-discrete element method with a novel and efficient contact activation scheme. *Int. J. Rock Mech. Min. Sci.* **2021**, *138*, 104645. [CrossRef]

36. Gao, W.; Liu, X.; Hu, J.; Feng, Y. A Novel Bilinear Constitutive Law for Cohesive Elements to Model the Fracture of Pressure-Dependent Rocks. *Rock Mech. Rock Eng.* **2022**, *55*, 521–540. [CrossRef]

37. Wang, B.; Li, H. Contribution of detonation gas to fracturing reach in rock blasting: Insights from the combined finite-discrete element method. *Comput. Part. Mech.* **2024**, *11*, 657–673. [CrossRef]

38. Bao, H.; Zhao, Z. Modeling brittle fracture with the nodal-based discontinuous deformation analysis. *Int. J. Comput. Methods* **2013**, *10*, 1350040. [CrossRef]

39. Tian, Q.; Zhao, Z.; Bao, H. Block fracturing analysis using nodal-based discontinuous deformation analysis with the double minimization procedure. *Int. J. Numer. Anal. Methods Geomech.* **2014**, *38*, 881–902. [CrossRef]

40. Sun, Y.; Feng, X.; Xiao, J.; Wang, Y. Discontinuous deformation analysis coupling with discontinuous Galerkin finite element methods for contact simulations. *Math. Probl. Eng.* **2016**, *2016*, 6217679. [CrossRef]

41. Yang, Y.; Wu, W.; Xu, D.; Xia, Y.; Yang, D. A nodal-based 3D discontinuous deformation analysis method with contact potential for discrete rock block system. *Rock Mech. Rock Eng.* **2023**, *56*, 4043–4059. [CrossRef]

42. Yang, Y.; Xia, Y. A nodal-based continuous-discontinuous deformation analysis method. *Comput. Methods Appl. Mech. Eng.* **2024**, *421*, 116790. [CrossRef]

43. Sun, Y.; Chen, Q.; Feng, X.; Wang, Y. Discontinuous deformation analysis enriched by the bonding block model. *Math. Probl. Eng.* **2015**, *2015*, 723263. [CrossRef]

44. Chen, H.; Zhang, Y.; Zhu, L.; Xiong, F.; Liu, J.; Gao, W. A Particle-Based Cohesive Crack Model for Brittle Fracture Problems. *Materials* **2020**, *13*, 3573. [CrossRef] [PubMed]

45. Augarde, C.E.; Deeks, A.J. The use of Timoshenko's exact solution for a cantilever beam in adaptive analysis. *Finite Elem. Anal. Des.* **2008**, *44*, 595–601. [CrossRef]

46. Mi, Y.; Crisfield, M.A.; Davies, G.; Hellweg, H. Progressive delamination using interface elements. *J. Compos. Mater.* **1998**, *32*, 1246–1272. [CrossRef]